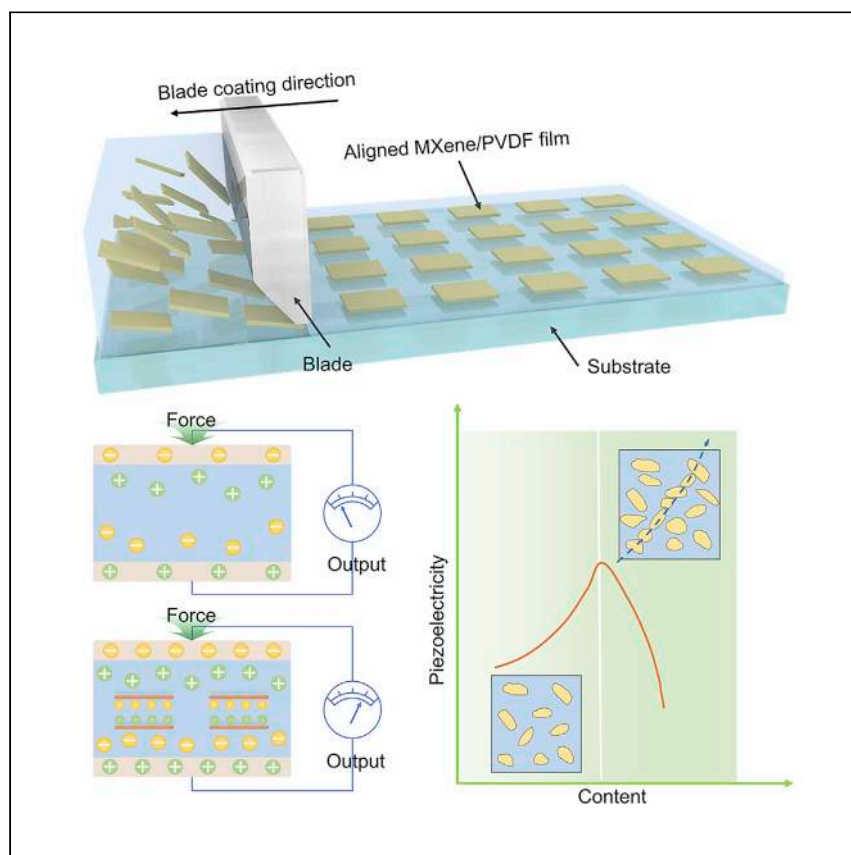


Article

# Dielectric micro-capacitance for enhancing piezoelectricity via aligning MXene sheets in composites



Tian et al. report an effective strategy to improve the piezoelectricity of composites via texturing well-aligned MXene sheets into PVDF. The device model is further put forward to uncover the underlying piezoelectric mechanisms and to motivate new design principles for the development of piezoelectric composites with improved performances.

Guo Tian, Weili Deng, Da Xiong, ..., Hongrui Zhang, Lin Deng, Weiqing Yang

wqyang@swjtu.edu.cn

Highlights

Composites with well-aligned fillers are fabricated via a scalable blade-coating method

The gap between dielectric properties and piezoelectricity in composites is narrowed

An appropriate model is put forward to guide the design of piezoelectric composites

Article

# Dielectric micro-capacitance for enhancing piezoelectricity via aligning MXene sheets in composites

Guo Tian,<sup>1,2</sup> Weili Deng,<sup>1,2</sup> Da Xiong,<sup>1,2</sup> Tao Yang,<sup>1</sup> Binbin Zhang,<sup>1</sup> Xiarong Ren,<sup>1</sup> Boling Lan,<sup>1</sup> Shen Zhong,<sup>1</sup> Long Jin,<sup>1</sup> Hongrui Zhang,<sup>1</sup> Lin Deng,<sup>1</sup> and Weiqing Yang<sup>1,3,\*</sup>

## SUMMARY

Piezoelectric polymers have attracted a great deal of attention for flexible electromechanical applications but still suffer from low piezoelectric coefficients ( $\sim -24$  pC/N) in commercial films. Here, we propose a dielectric micro-capacitance strategy to enhance piezoelectricity via texturing well-aligned MXene ( $\text{Ti}_3\text{C}_2\text{T}_x$ ) sheets into a poly(vinylidene fluoride) (PVDF) matrix using a scalable blade-coating technique. This aligned MXene/PVDF composite presents a piezoelectric coefficient of  $-63.3$  pC/N due to its improved permittivity. More importantly, a modified model of the piezo-composite is put forward to further understand the interfacial polarization and dielectric relaxation effect in this percolation system for designing piezo-composites with better performances. Notably, this work might motivate new design principles and approaches to regulate electric behavior and promote piezoelectricity in electroactive polymers.

## INTRODUCTION

Multiphase composite-engineering approaches, such as molecular doping, polymer grafting, or nanofillers co-blending, have been acknowledged as common strategies to improve dielectric and piezoelectric properties of electroactive polymers.<sup>1–7</sup> In this regard, various experiments and theories have been proposed to understand the underlying mechanisms of these processes, and some progress has been made in the last decades.<sup>8–15</sup> Regarding chemical components, trifluoroethylene (TrFE) is utilized to copolymerize with vinylidene fluoride (VDF). The tacticity of TrFE monomers will facilitate an order-to-disorder phase transition in poly(VDF) (PVDF), forming the so-called morphotropic phase boundary that exhibits an ultra-high piezoelectric coefficient ( $-63.5$  pC/N).<sup>1</sup> Compared with chemical modifications, physical methods are more suited to meet the low cost and scale requirements for real-life applications. Specifically, co-blending of polar inorganic nanoparticles with PVDF is a physical method to enhance piezoelectricity since the stronger polarity of the composite could induce the local orientation of  $\text{CH}_2\text{-CH}_2$  dipoles to form an all-trans TTT configuration, resulting in improved piezoelectricity ( $-33$  pC/N).<sup>16</sup> However, this rough co-blending strategy can hardly yield a sufficient performance improvement, and thus it is urgent to propose facile and high-efficiency strategies to promote the prosperity of piezoelectric polymers.

As per the classic description of the piezoelectric effect in piezoelectric polymers, the electrostriction model gives a quantitative reference of the piezoelectric coefficient as  $d_{33} = 2Q_{33}\epsilon_0\epsilon_r P_r$ , where  $d_{33}$  and  $Q_{33}$  are the piezoelectric and

<sup>1</sup>Key Laboratory of Advanced Technologies of Materials (Ministry of Education), School of Materials Science and Engineering, Southwest Jiaotong University, Chengdu 610031, P.R. China

<sup>2</sup>These authors contributed equally

<sup>3</sup>Lead contact

\*Correspondence: [wqyang@swjtu.edu.cn](mailto:wqyang@swjtu.edu.cn)  
<https://doi.org/10.1016/j.xcrp.2022.100814>

electrostrictive coefficients,  $\epsilon_0$  and  $\epsilon_r$  are the vacuum and relative permittivities, and  $P_r$  is the remnant polarization.<sup>17–19</sup> From this model, it is obvious that boosting  $Q_{33}$ ,  $\epsilon_r$ , and  $P_r$  can improve the piezoelectric coefficient. However, since the materials possess an abundance of polarization types,  $\epsilon_r$  could be tuned over a large scale, thus resulting in a higher piezoelectric coefficient compared with tuning  $Q_{33}$  and  $P_r$ .<sup>20</sup> For this purpose, the introduction of heterogeneous components is an effective method that could effectively promote the Maxwell-Wagner-Sillars polarization and thus increase the permittivity. Moreover, this polarization mainly depends on the difference in permittivity and the heterogeneous contact area between the two mediums.<sup>21,22</sup> Therefore, heterogeneous components with the greatest possible permittivity and aspect ratios are favorable to enhance the dielectric and piezoelectric properties. Accordingly, two-dimensional conductive materials with high aspect ratios have attracted sustained attention.<sup>23–26</sup> Among numerous two-dimensional materials, MXenes, equipped with numerous terminal groups, exhibit promising applications with tunable dielectric polarization and better compatibility in composites.<sup>27–29</sup> Due to the strong electrostatic interactions between MXene sheets and the polymer matrix, which can lock the polarization in fluoropolymers (presenting polarization-locking phenomena), the composite shows an excellent piezoelectric coefficient of  $-52$  pC/N.<sup>30</sup> In addition, the local dielectric micro-capacitance formed by micro-sized MXene sheets will enhance the dielectric properties of the composite and further improve its piezoelectricity.

In this work, a strategy of dielectric micro-capacitance-enhanced piezoelectricity is proposed via texturing well-aligned MXene ( $\text{Ti}_3\text{C}_2\text{T}_x$ ) sheets into a PVDF matrix using a scalable blade-coating technique. The dielectric micro-capacitance introduces the interfacial polarization that increases the permittivity, prompting a prominent improvement in piezoelectricity. This aligned MXene/PVDF composite presents an outstanding piezoelectric coefficient of  $-63.3$  pC/N. Moreover, a modified model for piezo-composites is proposed to further uncover the fundamental mechanism of interfacial polarization and dielectric relaxation effects in regulating piezoelectricity, which can contribute to establishing the principles for designing piezo-composites.

## RESULTS AND DISCUSSION

### Fabrication of $\text{Ti}_3\text{C}_2\text{T}_x$ /PVDF composite via blade coating

According to the schematic illustration of dielectric micro-capacitance-enhanced piezoelectricity (Figure 1A), the aligned texture of MXene sheets leads to stronger interfacial polarization than pure polymer matrix. Then, this device with dielectric micro-capacitance could generate a larger built-in electric field and release more induced charges during electromechanical conversion. Based on these analyses, a facile and efficient blade-coating technique was employed to fabricate a highly aligned MXene/PVDF composite film (Figure 1B). In this process, the shear-flow force was utilized to induce the alignment of MXene sheets, and the detailed experimental processes and principles are recorded in the Experimental procedures, Figure S1, and Note S5.<sup>31</sup> Composite films with different MXene contents were prepared for further performance studies, and the photographs of the resulting uniform large-area composite films are presented and discussed in Figure S2 and Note S6.

For this aligned MXene/PVDF composite film, Au electrodes were sputtered on the surfaces to collect the electrical output, and polyurethane (PU) was used to encapsulate the device to eliminate the interference from the external environment (Figure 1C). Furthermore, the morphology and structure characterizations were performed to validate the

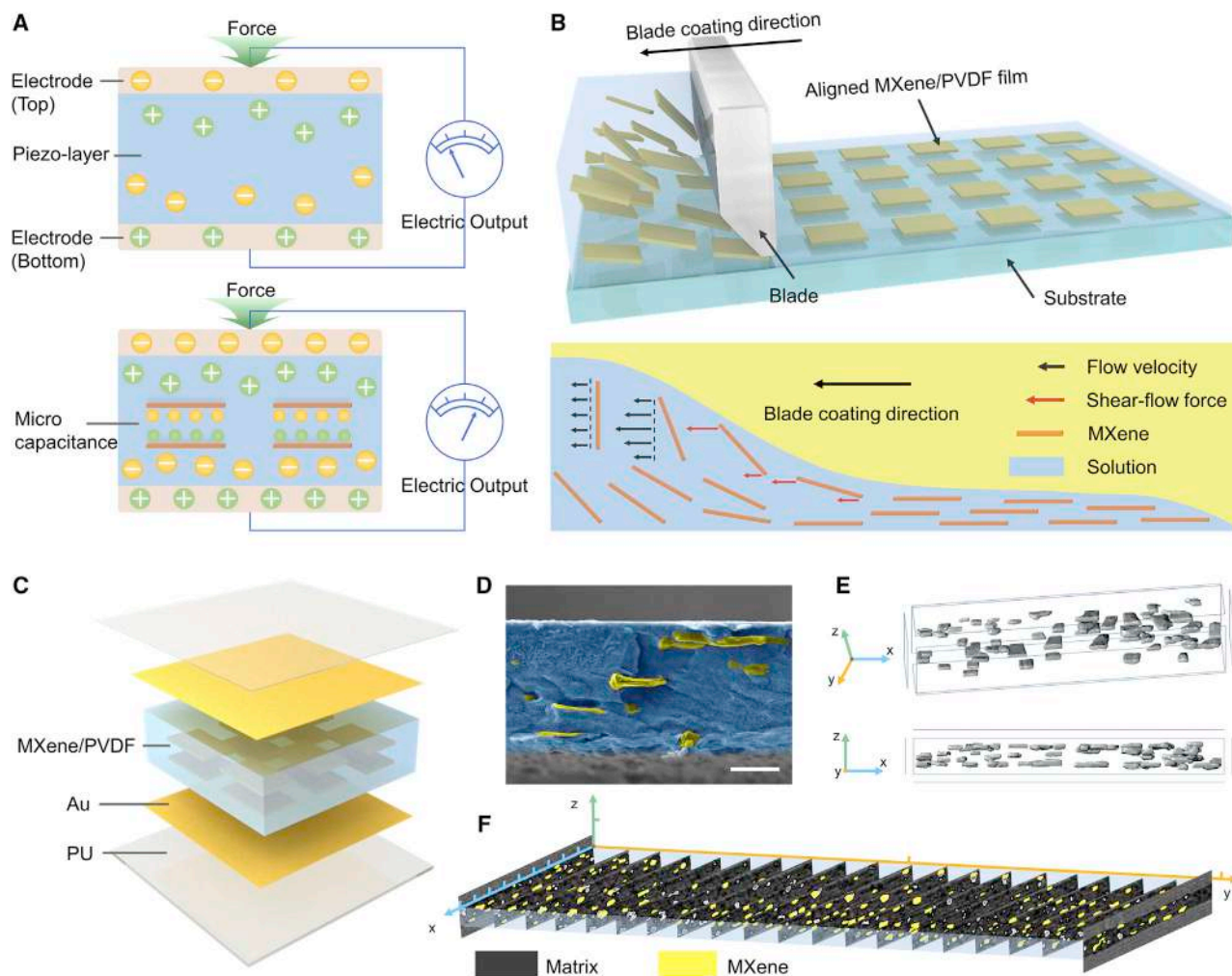


**Figure 1. Piezoelectric enhancement mechanism and fabrication process of the composite films featuring aligned MXene sheets**

(A) Schematic illustration of dielectric micro-capacitance-enhanced piezoelectricity.

(B) The blade-coating process (top panel) and theoretical schematic (bottom panel) of the shear-flow force-induced alignment of MXene sheets.

(C) The schematic diagram of MXene/PVDF-based piezoelectric device.

(D) The cross-section of MXene/PVDF composite film (scale bar is 10  $\mu\text{m}$ ).

(E) The reconstructed composite structure of the MXene/PVDF composite film is based on the results of nano-CT (three dimensional view and front view).

(F) The assembled selective sections of MXene/PVDF composite film were tested by nano-CT (each scale of the axes is 30  $\mu\text{m}$ ).

aligned structure of the prepared composites. As presented in [Figure S3](#) and [Note S7](#), the  $\text{Ti}_3\text{AlC}_2$  MAX phase was fully etched, a distinct layer-by-layer stacking structure was obtained with a lateral size from several to a dozen micrometers, and the intact crystal structure of  $\text{Ti}_3\text{C}_2\text{T}_x$  was clearly identified in the selected area electron diffraction pattern.<sup>32</sup> Besides, it could be clearly observed that the MXene sheets are arrayed in parallel through the cross section ([Figure 1D](#)). Furthermore, the nano X-ray computed tomography (nano-CT) characterization was employed to reconstitute this aligned structure of the MXene/PVDF composite. (The three-dimension model and partial results are presented in [Figures 1E](#) and [1F](#), and the details and partial original data are recorded and analyzed in the [Experimental procedures](#), [Figure S4](#), and [Note S8](#).) Combined with the structural evidence above, it can be concluded that the well-aligned MXene/PVDF composite films were successfully prepared via this blade-coating technique as per the previous design, which laid the foundation for the subsequent study.

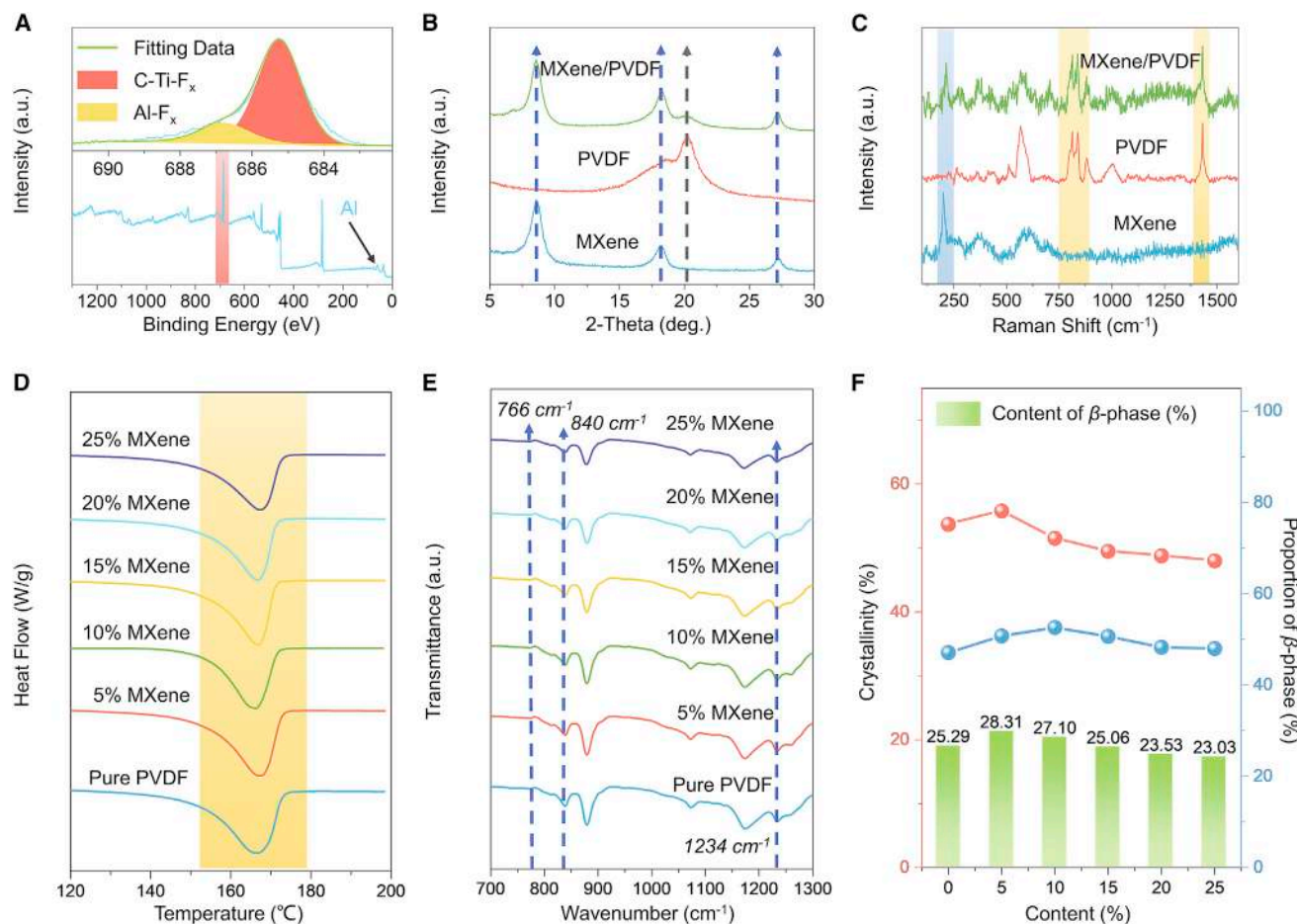


**Figure 2. Characterizations of the MXene/PVDF composite films**

(A) XPS survey spectra of MXene sheets on a silicon wafer and the binding energy values associated with F 1s.

(B and C) XRD scans (B) and Raman spectra (C) of MXene sheets on aluminum foil, free-standing PVDF, and MXene/PVDF (15%) composite films.

(D and E) Heat flow versus temperature testing (D) and infrared absorbance spectra (E) of MXene/PVDF composite films with MXene contents from 0% to 25%.

(F) The crystallinity of matrix, the proportion of  $\beta$ -phase (the proportion among  $\beta$ - and  $\gamma$ -phases in crystalline region) and content of  $\beta$ -phase (the total net content of  $\beta$ -phase in the crystal region) in the above samples vary with the contents of MXene.

### Structural and component characterizations of the composite

Except for morphology, the chemical composition of  $Ti_3C_2T_x$  was demonstrated by X-ray photoelectron spectroscopy (XPS) to make clear the terminal groups. The increased peaks of Ti 2p and C 1s confirm the successful etching of the MAX phase (Figures 2A and S5A, bottom; Note S9), and the F 1s peak (685.2 eV) indicates that this MXene sample contains abundant F-terminated Ti atoms (Figure 2A, top).<sup>33</sup> These F-terminated groups will vastly facilitate the formation of F–H-type hydrogen bonds and boost MXene sheets to be stably and uniformly dispersed in the PVDF matrix.<sup>27</sup> In Figures S5B and S5C, the presented peaks of C–Ti and Ti–O bonds further reveal the complete chemical composition of prepared  $Ti_3C_2T_x$ . These plentiful F-terminated groups ensure good compatibility and dispersibility of MXene in polymer matrix for texturing aligned composite structures.

Regarding these composite films, their components and structures were sufficiently understood and identified by X-ray diffraction (XRD) and Raman spectroscopy. In Figures 2B and S6, the XRD results reveal that the intensity of the characteristic

peak for MXene ( $2\theta = 7.2^\circ$ ) gradually heightens with increasing MXene contents (from 0% to 25%), while the PVDF matrix exhibits a distinct  $\beta$ -phase peak ( $2\theta = 20.26^\circ$ ); the contribution at a lower  $2\theta$  angle could be attributed to the larger out-of-plane lattice parameters of the  $\alpha$ - or  $\gamma$ -phase.<sup>16,34</sup> Furthermore, the proportion of different phases in PVDF is mainly the same (a detailed analysis is provided in [Note S10](#)). These results demonstrate that the phase structure of the polymer matrix has not been affected by the filler, and the Raman spectra show that the peak around  $205\text{ cm}^{-1}$  corresponds to the major peak of MXene,<sup>35</sup> with the latter two peaks appearing at  $813$  and  $840\text{ cm}^{-1}$ , indicating the presences of  $\gamma$ - and  $\beta$ -phases in the PVDF matrix ([Figure 2C](#)).<sup>36,37</sup> This structural evidence is reliably consistent with the above XRD patterns, and both results prove that structural integrity is still reserved during co-blending and blade coating.

In principle, both the piezoelectric  $\beta$ -phase of the polymer matrix and the interfacial polarization of dielectric micro-capacitance would contribute to piezoelectricity. Hence, it is necessary to quantitatively analyze the phase structure in the PVDF matrix to distinguish the dielectric contribution. For this, the crystallinities of composite films ([Figure 2F](#), red line) were tested with a differential scanning calorimeter (DSC) ([Figure 2D](#)).<sup>38</sup> The proportion of the  $\beta$ -phase in the crystal region (which was tested after etching the amorphous regions, and the method is recorded in the [Experimental procedures](#)) was measured by Fourier transform infrared spectroscopy ([Figure 2E](#)), and the calculated results are subsequently presented in [Figure 2F](#) (blue line; detailed calculations can be found in [Note S1](#)).<sup>39</sup> According to these characterizations, the contents of the  $\beta$ -phase are obtained ([Figure 2F](#), bar), and they are almost identical in all composite films. Therefore, it could be reasonably concluded that the piezoelectric differences will mainly come from the contribution of interfacial polarization.

### The analysis of piezoelectric contribution in $\text{Ti}_3\text{C}_2\text{T}_x/\text{PVDF}$ composite

In order to quantitatively evaluate the piezoelectric contribution produced by the dielectric micro-capacitance, the dielectric, ferroelectric, and piezoelectric properties were tested and analyzed following the electrostriction model. Concretely, the permittivities of composite films enlarge exponentially with increasing MXene contents, and the maximum value comes up to 46.4 at an MXene content of 25% ([Figure 3A](#)). Meanwhile, this exponential dependence among permittivity and content presumably corroborates the existence of percolation effect (detailed permittivity values are recorded in [Table S1](#)).<sup>6,22,40</sup> Besides, their polarization-electric field ( $P$ - $E$ ) curves were tested and discussed ([Figure S7](#); [Note S11](#)), and the induced and remnant polarizations were extracted to analyze the polarization behavior ([Figure 3B](#)). Noticeably, the induced polarization displays nonlinear variation, differing from the remnant polarization, and it presents a sharp increase at an MXene content of 15%. This is because the electrons will be more likely to migrate and form interfacial polarization under the polarization field once the MXene content reaches the critical percolative threshold of 15%. This phenomenon confirms the presence of a percolation effect once again.

After considering the permittivity and polarization, the electrostrictive coefficients were tested for calculating the  $d_{33}$  of the matrix.<sup>19</sup> From the  $P$ - $E$  and strain versus electric field ( $S$ - $E$ ) loops ([Figure S8](#)), the electrostriction of samples with different MXene contents was revealed, and we directly plot the strain as a function of polarization squared ( $P^2$ - $S$  curves; [Figure 3C](#)). According to the electrostriction model, the loops of that should be linear ([Note S2](#)). From the fitting line in [Figure 3C](#), the electrostriction coefficients of different samples were obtained for further calculations and analysis, as recorded in [Figure 3D](#).

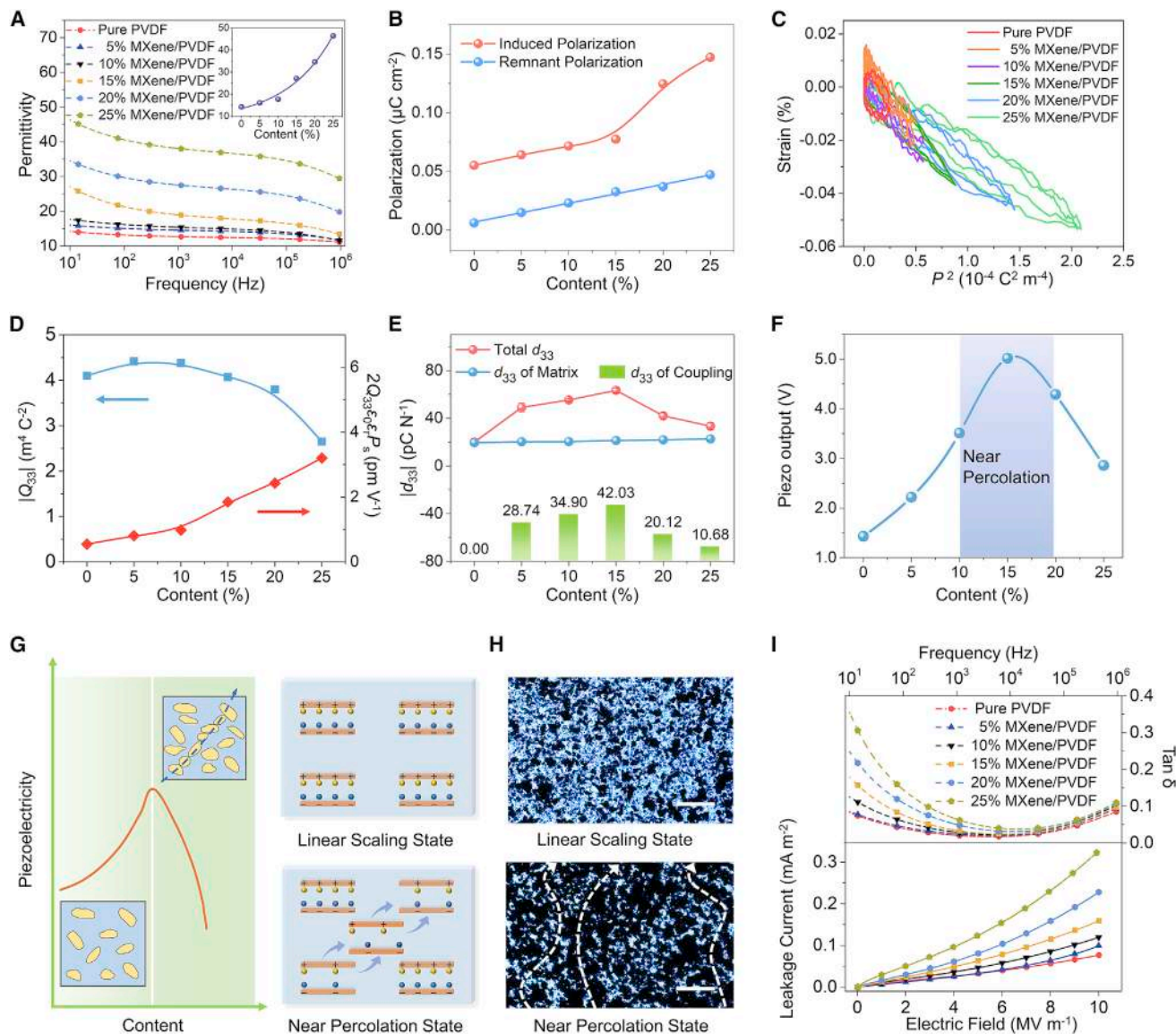


**Figure 3. Dielectric, ferroelectric, piezoelectric properties, and mechanism analysis of the MXene/PVDF composite films**

(A) Dielectric constants with different MXene contents under frequency from 10 to  $10^6$  Hz. The inset presents a fit of the constants in 10 Hz, indicating the percolation behavior.

(B) The induced and remnant polarization with different MXene contents at 10 MV/m electric field.

(C and D)  $P^2$ - $S$  curves (C) and the electrostrictive coefficients and the piezoelectric coefficients (D) of samples with different MXene contents.

(E) The calculated  $d_{33}$  of the Matrix is defined as the sum of the polymer matrix ( $d_{33\text{-matrixinter}}$ ) and electrostriction ( $2Q_{33}\epsilon_0\epsilon_r P_s$ ), the measured  $d_{33}$  (total  $d_{33}$ ) of the samples, and the coupling  $d_{33}$  of the interfacial polarization ( $d_{33}$  of coupling).

(F) The device piezo outputs of different composite films under 25 N force.

(G) Schematic of composites near the percolation threshold (left panel), the micro-capacitance percolation in the MXene/PVDF composite system, and the leakage current between capacitances (right panel).

(H) The optical microscope images of MXene/PVDF composite films are in linear scaling and near percolation states, respectively. The white lines in the bottom image indicate the percolation paths (the light and black regions represent the PVDF matrix and MXene sheets, respectively; scale bars are 100  $\mu\text{m}$ ).

(I) The frequency-dependent dielectric loss  $\tan \delta$  and the electric-field-dependent leakage current of various composite films.

Furthermore, the  $d_{33}$  of matrix phases were calculated via the electrostriction model (Figure 3E, blue line), and detailed data are recorded in Table S2. Meanwhile,  $d_{33}$  was measured by the quasi-static method (Figure 3E, red line), and

the principle of this method is illustrated in [Figure S9](#) and [Note S12](#). Apparently different from the results calculated above, the measured piezoelectric coefficient reaches up to  $-63.3$  pC/N at an MXene content of 15%. In order to explain this enormous difference, the composition of  $d_{33}$  was divided into three parts according to the electrostriction model ( $2Q_{33}\epsilon_0\epsilon_r P_r$ ), the interaction between crystal regions and amorphous regions ( $d_{33\text{-matrixinter}}$ ), and the contribution from the interfacial polarization of dielectric micro-capacitance ( $d_{33\text{-coupling}}$ ) (discussed in [Note S2](#)).<sup>19</sup> By comparing the theoretical and experimental results, it was found that the piezoelectricity from interfacial polarization ([Figure 3E](#), bar) was a crucial contribution far greater than that of the polymer matrix at a specific composite content ( $d_{33}$  of the matrix in [Figure 3E](#) was defined as the sum of the polymer matrix [ $d_{33\text{-matrixinter}}$ ] and electrostriction [ $2Q_{33}\epsilon_0\epsilon_r P_r$ ]). These results have certainly proven that the introduction of dielectric micro-capacitance is an extremely efficient approach to enhance piezoelectricity, and the optimized voltage output raises to 5.0 V ([Figure 3F](#)), showing an increase of 250% over that of pure PVDF (detailed results are plotted in [Figures S10](#) and [S11](#), and the linearity is demonstrated in [Note S13](#)). Interestingly, the  $d_{33}$  and the piezo outputs of the composite films show an abnormal decline under high MXene contents even with more interfacial polarization.

#### Interfacial polarization and dielectric relaxation in $\text{Ti}_3\text{C}_2\text{T}_x/\text{PVDF}$ composite

To illustrate this abnormal decline, the dielectric relaxation behavior was introduced into this percolative composite system. At low MXene contents, the dielectric micro-capacitance and concomitant interfacial polarization are beneficial to enhance the piezoelectricity of the composite. Upon exceeding the content threshold, the formation of conductive percolation paths would result in dielectric relaxation of polarization charges and a dramatic decline of piezoelectricity ([Figure 3G](#)).<sup>40</sup> Besides, according to the formula of piezoelectric voltage coefficient ( $g_{33} = d_{33}/\epsilon_{33}$ ; the derivation is recorded in [Note S3](#)), it is obvious that the voltage response is negatively correlated with the permittivity, and increasing permittivity will also lead to a decline of the piezoelectric voltage. [Figures 3H](#) and [S12](#) further show that this highly interconnected conductive structure was formed with MXene sheets. At low contents, the MXene sheets are discrete and isolated from each other. While exceeding the threshold of 15%, a continuous and conductive network forms throughout the whole film and provides percolation paths for the relaxation of polarization charges ([Figure 3H](#), white dotted lines, and discussion in [Note S14](#)), which leads to the abnormal decline of piezoelectricity at high MXene contents.

Moreover, dielectric losses and conductive behavior further prove this mechanism for the abnormal decline. As presented at high frequencies ([Figure 3I](#), top), the almost identical dielectric loss spectra originate from three intrinsic polarization losses of the molecular dipole, ions, and electrons, while at low frequencies, increasing dielectric losses with increasing MXene contents stem from extrinsic MXene/PVDF interfacial polarization. The highly interconnected MXene network provides lots of conductive paths for rapid electron migrating and then relaxing of interfacial polarization, causing the decline of piezoelectricity. In addition, [Figure S13](#), [Note S15](#), and [Table S3](#) demonstrate a typical exponential growth between conductivity and content, further confirming the formation of conductive percolation paths. Meanwhile, in the bottom part of [Figure 3I](#), when the MXene sheets exceed the critical content, the sharply increasing leakage current confirms the formation of highly interconnected MXene conductive paths. In a word, all these results make clear the

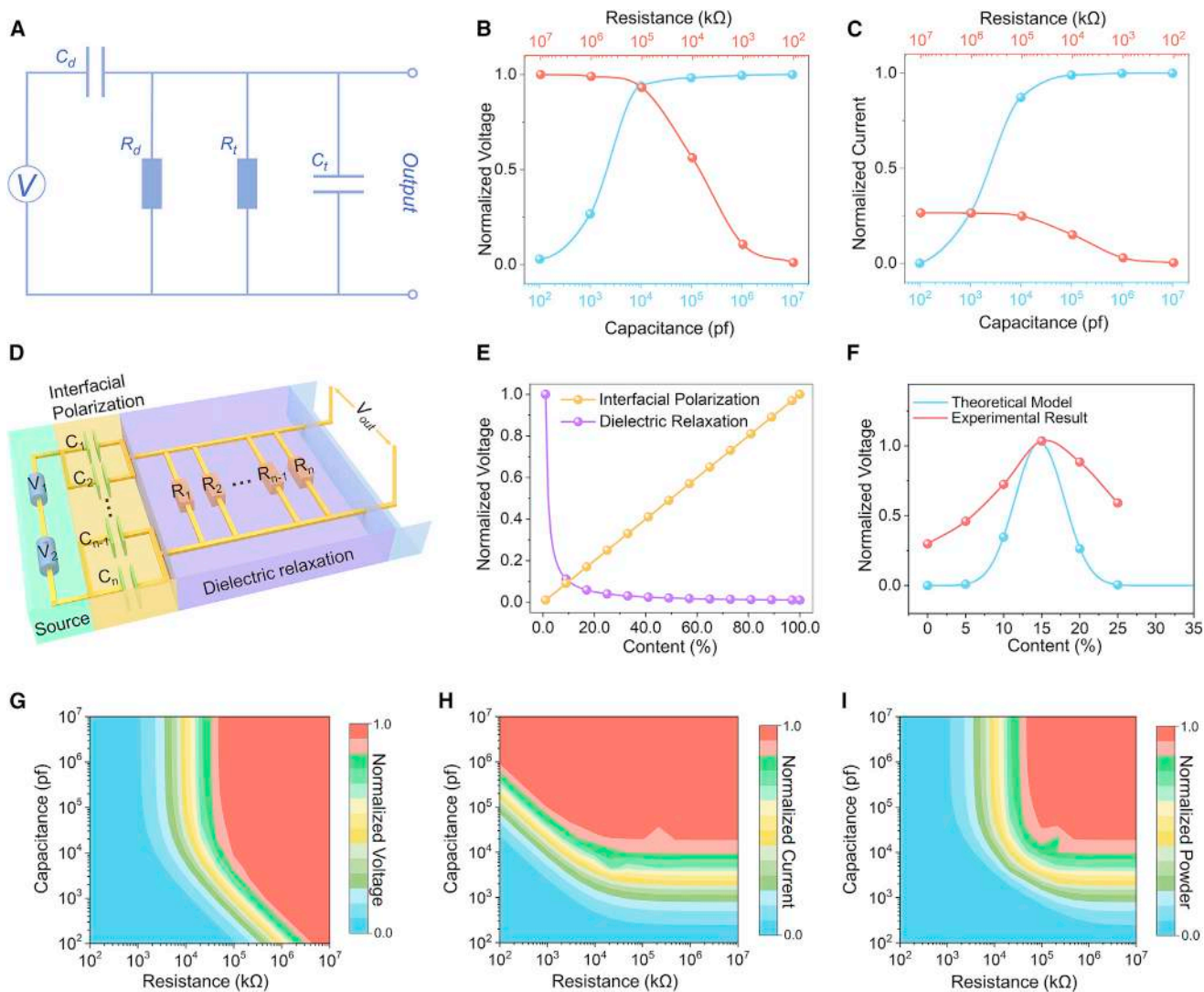


**Figure 4. Theoretical model analysis and evolution of composite-film-based piezo devices**

(A) The classic equivalent model of the piezo device and tested circuit. The  $C_d$ ,  $C_t$  and  $R_d$ ,  $R_t$  present the capacitance and resistance of the device and tested circuit, respectively.

(B and C) The computational voltage and current outputs of the device with different loading resistances and capacitances.

(D) The revised piezo model for this MXene/PVDF composite device.

(E) The schematic equilibrium between interfacial polarization and dielectric relaxation in the new model under incremental composite contents.

(F) Comparison of piezoelectric output between experimental results and theoretical models at different MXene contents.

(G–I) The instructive datasets of piezo voltage, current, and power outputs for designing composites.

competitive relationship between the micro-capacitance polarization and the dielectric relaxation-induced output recession.

### The revised piezoelectric model of the composite system

More generally, a piezoelectric device model was proposed to fully understand the fundamental regulation mechanism of the interfacial polarization and dielectric relaxation behaviors in order to design piezo-composites. As illustrated in Figure 4A, the output of the piezoelectric device is determined by the coupling among  $C_d$ ,  $R_d$  and  $C_t$ ,  $R_t$  (the capacitances and resistances of the device and the measuring circuit, respectively; details are discussed and calculated in Note S4). The introduction of

dielectric micro-capacitance greatly increases the  $C_d$  and decreases the  $R_d$ , corresponding to the trade-off between interfacial polarization and dielectric relaxation. On this ground, the piezo voltage and current outputs were simulated with different capacitances and resistances (Figures 4B and 4C; the resistance and capacitance are fixed at  $10^3$  pF and  $10^6$  k $\Omega$ , respectively, to scan another parameter). The results indicate that increasing dielectric micro-capacitance and restraining relaxation would be more beneficial to achieve better piezoelectricity. Meanwhile, the large capacitance favors an excellent current output.

Based on this model, a more thorough and accurate model was developed to describe the piezoelectric behavior of composite dielectric (Figure 4D). In this revised model, the piezoelectric contribution was divided into the intrinsic output of matrix ( $V_1$ ) and the polarization output of dielectric micro-capacitance ( $V_2$ ) to compensate for the deviation at low MXene contents. Then, the parallel capacitances and series resistors were adopted to model the interfacial polarization and dielectric relaxation caused by the conductive phase, respectively. Clearly, there will be an optimal content in keeping with the percolation threshold, where an equilibrium between interfacial polarization and dielectric relaxation is established (Figure 4E).

According to this revised model, a numerical model for voltage output based on the above trade-off was developed to provide theoretical references for comparison with the experimental results (Figure 4F; details are described in Note S4). Furthermore, a parameter sweep was applied to simulate the piezoelectric output of voltage, current, and power to predict the optimal composite content (Figures 4G–4I). With the help of a computational dataset (each pixel corresponds to a composite content), it was found that increasing the dielectric capacitance is more effective than suppressing the dielectric relaxation in improving piezoelectricity because increasing the dielectric capacitance endows the device with a greater applicable scale to obtain optimal piezo voltage and current outputs. To achieve an improved power output, both the resistance and dielectric capacitance must be as large as possible, implying that the piezoelectric composites must be sufficiently polarized with limited loss, which points to the development of composite dielectrics.

In summary, this study has provided advanced insights into the piezoelectric improvement of polymer-based composites. The experimental results validated that the piezoelectricity was enhanced due to the increased dielectric polarization generated by the dielectric micro-capacitance, promoting a piezoelectric coefficient of  $-63.3$  pC/N. More importantly, the interfacial polarization and dielectric relaxation behaviors were taken into account in the piezoelectric device model to understand the regulation mechanism in piezo-composites. This proposed modified model suggests that the piezoelectricity could be further improved by enhancing the interfacial polarization formed by micro-capacitance and restraining the dielectric relaxation derived from the conductive network. This work reveals a new way to understand the electric behavior of polymer composites and paves the way to exploit novel composites with outstanding piezoelectricity.

## EXPERIMENTAL PROCEDURES

### Resource availability

#### Lead contact

Further information and requests for resources and materials should be directed to and will be fulfilled by the lead contact, Weiqing Yang ([wqyang@swjtu.edu.cn](mailto:wqyang@swjtu.edu.cn)).

### Materials availability

All materials generated in this study will be made available upon reasonable request.

### Data and code availability

Details about the synthesis of materials and the data used to draw the conclusions can be found in the [Experimental procedures](#) and the [supplemental information](#). Requests for further data will be fulfilled by the lead contact.

### Preparation of the MXene sheets

The  $\text{Ti}_3\text{C}_2\text{T}_x$  sheets were synthesized by wet chemical etching of hydrofluoric acid (HF). In detail, the  $\text{Ti}_3\text{AlC}_2$  (2.5 g) powder was stirred magnetically at 40°C for 24 h with HF (25 mL 40 wt %) to break the Ti–Al–C bonds. Then, the product was washed with deionized water until the residual HF was totally removed until the pH value was over 6. The product was then dried to obtain  $\text{Ti}_3\text{C}_2\text{T}_x$  powder. After that, the obtained powder (90 mg) was dispersed into deionized water (30 mL) with ultrasonication treatment for 30 min. The dispersion liquid was then centrifuged at 3,500 RPM for 1 h (centrifugation force is about  $10,610 \times g$ ). The paste was collected through a vacuum suction filter from the upper suspension and then was dried under vacuum at 40 °C for 12 h (the vacuum degree of the oven was  $-0.1$  MPa) to obtain MXene-sheet powder.

### Fabrication of the composites with aligned MXene sheets

Firstly, the PVDF powders (Kynar 720, Arkema) were dissolved in 15 wt % *N,N*-dimethylformamide and stirred at 70°C for 3 h (all ratios are weight ratios in this work unless otherwise specified). Then, the prepared MXene sheets were mixed with this PVDF solution by stirring for 20 h to form a homogeneous dispersion, and the compound was placed in a vacuum box to exhaust air. The bubble-free compound was used in the blade-coating process, and the production was dried on the drying table at 40°C for 1 h then placed in the vacuum oven at 60°C for 10 h with a pressure of 1.325 kPa to obtain the MXene/PVDF composite film. The process of blade coating is described in the [supplemental information](#).

### Etching of the MXene/PVDF composites

The etching solution contained 30 g  $\text{P}_2\text{O}_5$ , 60 mL  $\text{H}_2\text{SO}_4$  (98%), and 0.3 g  $\text{Cr}_2\text{O}_3$ , and the mixed solution was heated to 90°C to dissolve the contents. Then, the sample was put into the etching liquid and kept at 90°C for 20 h to eliminate the amorphous regions in the samples. Finally, the etched samples were washed with deionized water 5 times and dried at 50°C for 1 h, then the processed samples were used for the Fourier transform infrared spectroscopy (FTIR).<sup>41</sup> Only the samples used for FTIR were etched, the other samples used for piezoelectric test were not etched, so the piezoelectric contribution in the latter contained the coupling of crystal and amorphous regions.

### Characterizations

Scanning electron microscopy (JSM 7800F) and transmission electron microscopy (JEM 2100F) were used to characterize the morphology and atom structure of composites and MXene. The accelerating voltage was 5.0 kV. The nano-CT results were obtained by SkyScan 2211 (Bruker). The resolution of the voxel was 500 nm, and the data were processed by the software of Dragonfly and Mimics 19.0. The XPS (ESCALAB XI +), XRD (Empyrean, PANalytical), Raman spectrum (HORIBA Jobin-Yvon XploRA ONE, 532 nm laser), differential scanning calorimetry (DSC; TGA/DSC 3+, Mettler Toledo), and FTIR (Nicolet 5700 Spectrometer) were applied to study the phase structure and crystal content for the PVDF, MXene, and composites. The dielectric properties were measured with a broad dielectric spectrometer

(Concept 80, Novocontrol) at room temperature, and the samples with Au electrodes were held by two copper cylinders. The ferroelectric and piezoelectric properties were tested by the TF Analyzer 3000 (aixACCT.) equipped with an amplifier (TREK MODEL) at room temperature with 10 Hz frequency, and the samples with Au electrodes were placed in silicone oil. Furthermore, the piezo output of devices was measured by a Keithley 6514, the pressure was applied by a linear motor (LinMot H01–23×86/160), and a force gauge (IMADA model ZPS-DPU-50N) was utilized to measure the pressure. The optical microscope images were captured by a Leica DM2700P (Leica Microsystem) instrument on transmission mode.

## SUPPLEMENTAL INFORMATION

Supplemental information can be found online at <https://doi.org/10.1016/j.xcrp.2022.100814>.

## ACKNOWLEDGMENTS

This research was financially supported by the National Natural Science Foundation of China (no. 61801403); the Sichuan Province Foundation for Distinguished Young Team (no. 20CXTD0106); the Sichuan Science and Technology Program (no. 2020YFG0370); the Postgraduate Scientific Research & Innovation Competition Project of Southwest Jiaotong University (no. 2021KCJS66); the Opening Project of State Key Laboratory of Polymer Materials Engineering (Sichuan University) (no. SKLPME2019-4-27); and the Basic Research Cultivation Project (no. 2682021ZTPY004). We are thankful for help from the Analysis and Testing Center of Southwest Jiaotong University.

## AUTHOR CONTRIBUTIONS

G.T., W.D., and D.X. contributed equally to this work; G.T., W.D., D.X., and W.Y. designed the research; G.T. and D.X. prepared the materials and devices; W.D., T.Y., B.Z., X.R., L.J., and S.Z. carried out the data and mechanism analyses; H.Z., B.L., and L.D. developed the property tests; G.T. and W.D. organized the data and wrote the original manuscript; all authors reviewed and commented on the paper.

## DECLARATION OF INTERESTS

The authors declare no competing interests.

Received: October 6, 2021

Revised: January 2, 2022

Accepted: February 23, 2022

Published: March 17, 2022

## REFERENCES

1. Liu, Y., Aziguli, H., Zhang, B., Xu, W., Lu, W., Bernholc, J., and Wang, Q. (2018). Ferroelectric polymers exhibiting behaviour reminiscent of a morphotropic phase boundary. *Nature* 562, 96–100.
2. Terzic, I., Meereboer, N.L., Acuautila, M., Portale, G., and Loos, K. (2019). Electroactive materials with tunable response based on block copolymer self-assembly. *Nat. Commun.* 10, 601.
3. Li, Q., Chen, L., Gadinski, M.R., Zhang, S., Zhang, G., Li, U., Iagodkine, E., Haque, A., Chen, L.Q., Jackson, N., and Wang, Q. (2015). Flexible high-temperature dielectric materials from polymer nanocomposites. *Nature* 523, 576–579.
4. Liu, Y., Zhang, B., Xu, W., Haibibu, A., Han, Z., Lu, W., Bernholc, J., and Wang, Q. (2020). Chirality-induced relaxor properties in ferroelectric polymers. *Nat. Mater.* 19, 1169–1174.
5. Dang, Z.M., Yuan, J.K., Yao, S.H., and Liao, R.J. (2013). Flexible nanodielectric materials with high permittivity for power energy storage. *Adv. Mater.* 25, 6334–6365.
6. Dang, Z.M., Yuan, J.K., Zha, J.W., Zhou, T., Li, S.T., and Hu, G.H. (2012). Fundamentals, processes and applications of high-permittivity polymer-matrix composites. *Prog. Mater. Sci.* 57, 660–723.
7. Yang, T., Pan, H., Tian, G., Zhang, B.B., Xiong, D., Gao, Y.Y., Yan, C., Chu, X., Chen, N., Zhong, S., et al. (2020). Hierarchically structured PVDF/ZnO core-shell nanofibers for self-powered physiological monitoring electronics. *Nano Energy* 72, 104706.
8. Hafner, J., Benaglia, S., Richeimer, F., Teuschel, M., Maier, F.J., Werner, A., Wood, S.,

- Platz, D., Schneider, M., Hradil, K., et al. (2021). Multi-scale characterisation of a ferroelectric polymer reveals the emergence of a morphological phase transition driven by temperature. *Nat. Commun.* **12**, 152.
9. Huang, Y., Rui, G., Li, Q., Allahyarov, E., Li, R., Fukuto, M., Zhong, G.J., Xu, J.Z., Li, Z.M., Taylor, P.L., and Zhu, L. (2021). Enhanced piezoelectricity from highly polarizable oriented amorphous fractions in biaxially oriented poly(vinylidene fluoride) with pure  $\beta$  crystals. *Nat. Commun.* **12**, 675.
  10. Liu, Y., Yang, T., Zhang, B., Williams, T., Lin, Y.T., Li, L., Zhou, Y., Lu, W., Kim, S.H., Chen, L.Q., et al. (2020). Structural insight in the interfacial effect in ferroelectric polymer nanocomposites. *Adv. Mater.* **32**, 2005431.
  11. Peng, S.M., Yang, X., Yang, Y., Wang, S., Zhou, Y., Hu, J., Li, Q., and He, J.L. (2019). Direct detection of local electric polarization in the interfacial region in ferroelectric polymer nanocomposites. *Adv. Mater.* **31**, 1807722.
  12. Pourrahimi, A.M., Olsson, R.T., and Hedenqvist, M.S. (2018). The role of interfaces in polyethylene/metal-oxide nanocomposites for ultrahigh-voltage insulating materials. *Adv. Mater.* **30**, 1703624.
  13. Deng, W.L., Yang, T., Jin, L., Yan, C., Huang, H.C., Chu, X., Wang, Z.X., Xiong, D., Tian, G., Gao, Y.Y., et al. (2019). Cowpea-structured PVDF/ZnO nanofibers based flexible self-powered piezoelectric bending motion sensor towards remote control of gestures. *Nano Energy* **55**, 516–525.
  14. Tian, G., Deng, W.L., Gao, Y.Y., Xiong, D., Yan, C., He, X., Yang, T., Jin, L., Chu, X., Zhang, H., et al. (2019). Rich lamellar crystal baklava-structured PZT/PVDF piezoelectric sensor toward individual table tennis training. *Nano Energy* **59**, 574–581.
  15. Liu, Y., Lin, Y., Haibibu, A., Xu, W.H., Zhou, Y., Li, L., Kim, S.H., and Wang, Q. (2021). Relaxor ferroelectric polymers: insight into high electrical energy storage properties from a molecular perspective. *Small Sci.* **1**, 2000061.
  16. Martins, P., Lopes, A.C., and Lanceros-Mendez, S. (2014). Electroactive phases of poly(vinylidene fluoride): determination, processing and applications. *Prog. Polym. Sci.* **39**, 683–706.
  17. Takeo, F., and Naoya, S. (1990). Electrostriction as the origin of piezoelectricity in ferroelectric polymers. *Jap. J. Appl. Phys.* **29**, 675–680.
  18. Liu, Y., and Wang, Q. (2020). Ferroelectric polymers exhibiting negative longitudinal piezoelectric coefficient: progress and prospects. *Adv. Sci.* **7**, 1902468.
  19. Katsouras, I., Asadi, K., Li, M., Driel, T.B., Kjaer, K.S., Zhao, D., Lenz, T., Gu, Y., Blom, P.W., Damjanovic, D., et al. (2016). The negative piezoelectric effect of the ferroelectric polymer poly(vinylidene fluoride). *Nat. Mater.* **15**, 78–84.
  20. Fan, B., Zhou, M., Zhang, C., He, D., and Bai, J. (2019). Polymer-based materials for achieving high energy density film capacitors. *Prog. Polym. Sci.* **97**, 101143.
  21. Prateek, Thakur, V.K., and Gupta, R.K. (2016). Recent progress on ferroelectric polymer-based nanocomposites for high energy density capacitors: synthesis, dielectric properties, and future aspects. *Chem. Rev.* **116**, 4260–4317.
  22. He, F., Lau, S., Chan, H.L., and Fan, J. (2009). High dielectric permittivity and low percolation threshold in nanocomposites based on poly(vinylidene fluoride) and exfoliated graphite nanoplates. *Adv. Mater.* **21**, 710–715.
  23. Wei, Q.W., Pei, S.F., Qian, X.T., Liu, H.P., Liu, Z.B., Zhang, W.M., Zhou, T.Y., Zhang, Z.C., Zhang, X.F., Cheng, H.M., and Ren, W.C. (2020). Superhigh electromagnetic interference shielding of ultrathin aligned pristine graphene nanosheets film. *Adv. Mater.* **32**, 1907411.
  24. Hantanasirisakul, K., and Gogotsi, Y. (2018). Electronic and optical properties of 2D transition metal carbides and nitrides (MXenes). *Adv. Mater.* **30**, 1804779.
  25. Shahzad, F., Alhabeb, M., Hatter, C.B., Anasori, B., Hong, S.M., Koo, C.M., and Gogotsi, Y. (2016). Electromagnetic interference shielding with 2D transition metal carbides (MXenes). *Science* **353**, 1137–1140.
  26. Iqbal, A., Shahzad, F., Hantanasirisakul, K., Kim, M.K., Kwon, J., Hong, J., Kim, H., Kim, D., Gogotsi, Y., and Koo, C.M. (2020). Anomalous absorption of electromagnetic waves by 2D transition metal carbonitride  $Ti_3C_2Tx$  (MXene). *Science* **369**, 446–450.
  27. Tu, S.B., Jiang, Q., Zhang, X.X., and Alshareef, H.N. (2018). Large dielectric constant enhancement in MXene percolative polymer composites. *ACS Nano* **12**, 3369–3377.
  28. Anasori, B., Lukatskaya, M.R., and Gogotsi, Y. (2017). 2D metal carbides and nitrides (MXenes) for energy storage. *Nat. Rev. Mater.* **2**, 16098.
  29. Hart, J.L., Hantanasirisakul, K., Lang, A.C., Anasori, B., Pinto, D., Pivak, Y., Omme, J.T., May, S.J., Gogotsi, Y., and Taheri, M.L. (2019). Control of MXenes' electronic properties through termination and intercalation. *Nat. Commun.* **10**, 522.
  30. Shepelin, N.A., Sherrell, Peter.C., Skountzos, E.N., Goudeli, E., Zhang, J.Z., Lussini, V.C., Imtiaz, B., Usman, K.A.S., Dicoski, G.W., Shapter, J.G., et al. (2021). Interfacial piezoelectric polarization locking in printable  $Ti_3C_2Tx$  MXene-fluoropolymer composites. *Nat. Commun.* **12**, 3171.
  31. Zhang, J.Z., Kong, N., Uzun, S., Levitt, A., Seyedin, S., Lynch, P.A., Qin, S., Han, M., Yang, W., Liu, J., et al. (2020). Scalable manufacturing of free-standing, strong  $Ti_3C_2Tx$  MXene films with outstanding conductivity. *Adv. Mater.* **32**, 2001093.
  32. Naguib, M., Mashtalir, O., Carle, J., Presser, V., Lu, J., Hultman, L., Gogotsi, Y., and Barsoum, M.W. (2012). Two-dimensional transition metal carbides. *ACS Nano* **6**, 1322–1331.
  33. Halim, J., Cook, K.M., Naguib, M., Eklund, P., Gogotsi, Y., Rosen, J., and Barsoum, M.W. (2016). X-ray photoelectron spectroscopy of select multi-layered transition metal carbides (MXenes). *Appl. Surf. Sci.* **362**, 406–417.
  34. Naguib, M., Kurtoglu, M., Presser, V., Lu, J., Niu, J., Heon, M., Hultman, L., Gogotsi, Y., and Barsoum, M.W. (2011). Two-dimensional nanocrystals produced by exfoliation of  $Ti_3AlC_2$ . *Adv. Mater.* **23**, 4248–4253.
  35. Sarycheva, A., and Gogotsi, Y. (2020). Raman spectroscopy analysis of the structure and surface chemistry of  $Ti_3C_2Tx$  MXene. *Chem. Mater.* **32**, 3480–3488.
  36. Li, T., Feng, Z.Q., Qu, M., Yan, K., Yuan, T., Gao, B., Wang, T., Dong, W., and Zheng, J. (2019). Core/shell piezoelectric nanofibers with spatial self-orientated  $\beta$ -phase nanocrystals for real-time micropressure monitoring of cardiovascular walls. *ACS Nano* **13**, 10062–10073.
  37. Zhang, S.N., Wang, H., Xu, D.G., Yang, W.X., Tang, P., and Bin, Y.Z. (2016). Study of crystallization behavior of neat poly(vinylidene fluoride) and transcrystallization in carbon fiber/poly(vinylidene fluoride) composite under a temperature gradient. *J. Appl. Polym. Sci.* **133**, 43605.
  38. Shepelin, N.A., Glushenkov, A.M., Lussini, V.C., Fox, P.J., Dicoski, G.W., Shapter, J.G., and Ellis, A.V. (2019). New developments in composites, copolymer technologies and processing techniques for flexible fluoropolymer piezoelectric generators for efficient energy harvesting. *Energy Environ. Sci.* **12**, 1143–1176.
  39. Meng, N., Ren, X., Santagiuliana, G., Ventura, L., Zhang, H., Wu, J., Yan, H., Reece, M.J., and Bilotti, E. (2019). Ultrahigh  $\beta$ -phase content poly(vinylidene fluoride) with relaxor-like ferroelectricity for high energy density capacitors. *Nat. Commun.* **10**, 4535.
  40. Nan, C.W., Shen, Y., and Ma, J. (2010). Physical properties of composites near percolation. *Annu. Rev. Mater. Res.* **40**, 131–151.
  41. Jin, L., Ma, S.Y., Deng, W.L., Yan, C., Yang, T., Chu, X., Tian, G., Xiong, D., Lu, J., and Yang, W.Q. (2018). Polarization-free high-crystallization  $\beta$ -PVDF piezoelectric nanogenerator toward self-powered 3D acceleration sensor. *Nano Energy* **50**, 632.